Brain, Behavior, & Immunity - Health 21 (2022) 100451

Contents lists available at ScienceDirect

Brain, Behavior, & Immunity - Health

journal homepage: www.editorialmanager.com/bbih/default.aspx

Pathological consequences of chronic olfactory inflammation on neurite morphology of olfactory bulb projection neurons

Brandon J. LaFever [a], Yuka Imamura Kawasawa [a,b,c], Ayako Ito [a], Fumiaki Imamura [a,*]

[a] Department of Pharmacology, Penn State College of Medicine, 500 University Dr., Hershey, PA, 17033, USA
[b] Department of Biochemistry and Molecular Biology, Penn State College of Medicine, 500 University Dr., Hershey, PA, 17033, USA
[c] Institute for Personalized Medicine, Penn State College of Medicine, 500 University Dr., Hershey, PA, 17033, USA

ARTICLE INFO

Keywords:
Chronic rhinosinusitis
Chronic olfactory inflammation
Olfactory system
Projection neurons
Neurite
Lipopolysaccharide

ABSTRACT

Chronic olfactory inflammation (COI) in conditions such as chronic rhinosinusitis significantly impairs the functional and anatomical components of the olfactory system. COI induced by intranasal administration of lipopolysaccharide (LPS) results in atrophy, gliosis, and pro-inflammatory cytokine production in the olfactory bulb (OB). Although chronic rhinosinusitis patients have smaller OBs, the consequences of olfactory inflammation on OB neurons are largely unknown. In this study, we investigated the neurological consequences of COI on OB projection neurons, mitral cells (MCs) and tufted cells (TCs). To induce COI, we performed unilateral intranasal administration of LPS to mice for 4 and 10 weeks. Effects of COI on the OB were examined using RNA-sequencing approaches and immunohistochemical analyses. We found that repeated LPS administration upregulated immune-related biological pathways in the OB after 4 weeks. We also determined that the length of TC lateral dendrites in the OB significantly decreased after 10 weeks of COI. The axon initial segment of TCs decreased in number and in length after 10 weeks of COI. The lateral dendrites and axon initial segments of MCs, however, were largely unaffected. In addition, dendritic arborization and AIS reconstruction both took place following a 10-week recovery period. Our findings suggest that olfactory inflammation specifically affects TCs and their integrated circuitry, whereas MCs are potentially protected from this condition. This data demonstrates unique characteristics of the OBs ability to undergo neuroplastic changes in response to stress.

1. Introduction

Individuals are exposed to chemicals and environmental agents on a daily basis, some of which are capable of entering the body and inducing an immune response. Bacteria, viruses, and allergens such as dust, mold, or pollen are common agents that can enter the nasal cavity and induce inflammation of the olfactory mucosa (OM), mucous membranes lining the olfactory epithelium (OE), and the paranasal sinuses (Peters et al., 2014; Ahmad and Zacharek, 2008). This inflammatory state is the foundation to the disease known as rhinosinusitis (Patel and Pinto, 2014). Rhinosinusitis is one of the most common medical conditions in the world (Rosenfeld et al., 2015), currently affecting about 12.5% of individuals in the United States alone (Hamilos, 2011). Symptoms of rhinosinusitis can include thick nasal mucus, stuffy nose and congestion, facial pain, headache, cough, fever, and hyposmia/anosmia (Dalton; Doty and Mishra, 2001; Meltzer et al., 2004). Rhinosinusitis can be an acute or chronic disease (Gudis and Soler, 2016; Sánchez-Vallecillo et al., 2012), yet when the condition lasts longer than 12 weeks it is considered chronic rhinosinusitis (CRS) and is typically due to a bacterial infection (Rosenfeld et al., 2015; Meltzer et al., 2004; Gwaltney, 1996; Benninger et al., 2003).

Although immune responses are an essential first line of defense for the body against invading pathogens, chronic inflammation can act as a significant stressor on an organ or system and may result in damage of the affected tissue (DiSabato et al., 2016; Kotas Maya and Medzhitov, 2015; Skaper et al., 2018). Although airflow obstruction within the nasal cavity has been linked to hyposmia, clinical studies have demonstrated that the immune response induced during CRS can severely damage the OM and OE, another major contributor to the loss of smell (Kern, 2000; Lanza and Kennedy, 1997; Wolfensberger and Hummel, 2002; Yee et al., 2009). Patients with CRS also exhibit a decrease in the volumetric size of their olfactory bulbs (OBs) (Alarabawy et al., 2016; Rombaux et al., 2008). Nonetheless, the extent to which the CRS-induced inflammatory responses affect the central nervous system (CNS) including the OB is currently not well understood.

* Corresponding author. Department of Pharmacology, Penn State College of Medicine, 500 University Drive, Hershey, PA, 17033, USA.
E-mail address: fui1@psu.edu (F. Imamura).

https://doi.org/10.1016/j.bbih.2022.100451
Received 7 January 2022; Received in revised form 10 March 2022; Accepted 12 March 2022
Available online 18 March 2022

Preclinical research using rodents has established that intranasal (i.n.) administration of various chemical entities can induce inflammation of the OE in the form of immune cell activation, infiltration, and pro-inflammatory cytokine release resulting in apoptosis of olfactory sensory neurons (OSNs) (Epstein et al., 2008; Hasegawa-Ishii et al., 2017; Islam et al., 2006, 2007; Kanaya et al., 2014; Lindsay et al., 2006; Yagi et al., 2007). Our previous studies have also demonstrated that i.n. administration of lipopolysaccharide (LPS) has severe implications on the CNS including OB gliosis and atrophy (Hasegawa-Ishii et al., 2017, 2019, 2020). More specifically, beginning as early as 3 weeks of i.n. LPS administrations, a significant upregulation of microglial and astrocytic activity as well as the presence of pro-inflammatory cytokines can be detected in the superficial OB layers including the olfactory nerve layer (ONL), glomerular layer (GL), and the superficial external plexiform layer (sEPL). Interestingly, after 10 weeks of administrations, OB atrophy takes place primarily in the same three superficial OB layers in which the layers are significantly thinner than in controls (Hasegawa-Ishii et al., 2019, 2020).

Olfactory information is relayed from the OE in the nose by the OSNs which project their axons to the OB in the CNS. OSN axons innervate glomeruli in the OB. In order for an organism to fully process the olfactory sensation, the information must be transmitted to the olfactory cortex (OC). The transfer of olfactory information from the OB to the OC is carried out by two types of OB projection neurons known as tufted (TC) and mitral (MC) cells. Although TCs and MCs are both excitatory, glutamatergic projection neurons, TC somata are located in the EPL and extend their lateral dendrites throughout the sEPL, whereas MC somata exist in the MCL and extend their lateral dendrites in the dEPL (Nagayama et al., 2014; Igarashi et al., 2012; Orona et al., 1984). Similarly, the axons of MCs and TCs differ in their projection patterns in which TCs target the more anterior portion of the OC including the anterior olfactory nucleus, olfactory tubercle, and anterior piriform cortex (Igarashi et al., 2012; Orona et al., 1984; Chon et al., 2020; Mori and Sakano, 2011), whereas MCs target the entire OC (Nagayama et al., 2014; Chon et al., 2020). MCs and TCs also differ in their physiological response to glomerular stimulation in which the firing frequencies of MCs are significantly lower than that of TCs (Nagayama et al., 2004). The anatomical and physiological differences between MCs and TCs suggests that their response to a state of chronic inflammation may also differ based on divergent cellular properties.

In this study, and in conjunction with our previous studies, we administered LPS into the mouse nostril repetitively over the course of 4 and 10 weeks to induce a state of chronic inflammation of the OE (or chronic olfactory inflammation, COI). We report that COI induces a decrease in the activity of projection neurons residing in the EPL (TCs), as well as dendritic retraction and axonal instability of the same neurons. MCs residing in the mitral cell layer (MCL), however, appear to be almost entirely unaffected. Finally, we report that the COI-induced TC impairments return to homeostasis following a recovery period. These results provide further evidence that the OB consists of highly plastic components capable of undergoing severe stress.

2. Materials and methods

2.1. Animals

In this study, we used C57BL/6J (stock #000664) and YFP knockin (stock #006148; C57BL/6J background) mice purchased from The Jackson Laboratory, as well as Pcdh21-CreER knockin (BRC #RBRC02410; C57BL/6J background) mice purchased from Riken BRC. Pcdh21-CreER x YFP mice were created by crossing Pcdh21-CreER-positive mice with YFP homozygotes to create Cre-positive/YFP heterozygotes (+/Het mice; this was the only genotype used for this mouse line in this study). Among the +/Het mice, a yellow fluorescent protein, YFP, is specifically expressed in MCs/TCs in the OBs following tamoxifen injections. All mice were deeply anesthetized with isoflurane and intranasally administered 10 μL of lipopolysaccharide (LPS) from *Escherichia coli* (Sigma; product #L2880; lot #025M4040V) in physiologic saline (10 μg; 1 mg/ml x 10 μl), which causes the inflammatory responses in the OE (Hasegawa-Ishii et al., 2017, 2019, 2020). LPS administrations took place three times per week for 4 or 10 weeks and were carried out unilaterally to the left naris of each mouse, with the right side serving as an internal control. Our previous studies of LPS-induced COI demonstrated that OB gliosis was detected at the 3-week time point (Hasegawa-Ishii et al., 2017) whereas OB atrophy was first observed at the 10-week time point (Hasegawa-Ishii et al., 2019), and thus we use the 4- and 10-week time points for our RNA-sequencing and immunohistochemical analyses, respectively.

All mice used in this study were male and eight weeks old at the start of LPS administrations; one group of C57BL6/J mice (n = 3) for the RNA-sequencing analysis; one group of +/Het mice (n = 3) was used to investigate OB projection neuron lateral dendrites; one group of C57BL6/J mice (n = 5) was used for the remaining immunohistochemical analyses at the 10-week time point. For analyses of recovery, one group of eight-week-old +/Het mice (n = 3) underwent the unilateral 10-week LPS administration paradigm and were subsequently housed for 10 weeks with no additional treatment. In the present study, we only used the laboratory mice that had exactly the same genetic background and were housed in exactly the same environment. We repeated the experiments using at least 3 different animals, which is the same design as in our previous study using similar i.n. LPS administration techniques (Hasegawa-Ishii et al., 2017, 2019). Although the sample size might be smaller than that estimated using a power analysis, the current and previous findings indicated that the data obtained did not vary widely among the mice within the same experimental group. Therefore, numbers of animals used in this study were sufficient to be subjected to a statistical analysis.

Three days prior to being sacrificed for immunohistochemical analyses, mice were first injected (i.p.) with tamoxifen (30 mg/kg). The dose for tamoxifen was selected after multiple trials at different doses in order to observe optimal YFP expression in fewer OB projection neurons allowing us to trace individual neuron apical and lateral dendrites (data not shown). For histologic preparation, mice were anesthetized with ketamine (100 mg/kg) and xylazine (10 mg/kg) and transcardially perfused with PBS, followed by 4% (wt/vol) paraformaldehyde in PBS. Heads were removed and placed in the same fixative at 4 °C overnight. The rostral half of the calvaria (anterior to the bregma) and the nasal bone were then placed in 0.45 mol/L EDTA in PBS at 4 °C for 2 days for decalcification, cryoprotected with 30% sucrose (wt/vol) at 4 °C overnight, embedded in OCT compound (Sakura Finetek USA, Torrance, Calif), and maintained at −80 °C until use. All protocols were approved by and all methods were performed in accordance with the guidelines of the Institutional Animal Care and Use Committee of Penn State College of Medicine.

2.2. RNA sequencing analysis

2.2.1. RNA extraction

OBs were microdissected from fixed and cryopreserved whole mouse brains. Approximately 5 mg of frozen tissue was incubated with proteinase K (500 μg/ml) in 500 μl of 10 mM NaCl, 500 mM Tris (pH 8.0), 20 mM EDTA, and 1% SDS at 55 °C for 3 h until the tissue was completely dissolved (Körbler et al., 2003). The acid phenol-chloroform method was applied for RNA extraction using the Direct-zol™ RNA Micro prep Kit (Zymo Research). RNA quality and quantity were determined by RNA Pico BioAnalyzer (Agilent technologies). The average RNA Integrity Number (RIN) value was 2.2.

2.2.2. RNA-sequencing and analysis

The cDNA libraries were prepared using the QuantSeq 3'mRNA-Seq Library Prep Kit FWD for Illumina (Lexogen) as per the manufacturer's instructions. The QuantSeq FWD Kit is designed to generate Illumina compatible libraries of sequences close to the 3′ end of polyadenylated

RNA and is proven to be suitable for degraded RNA from fixed tissue samples (Jang et al., 2021). Briefly, total RNA at 20–50 ng in mass was reverse transcribed using oligo (dT) primers. The second cDNA strand was synthesized by random priming, in which DNA polymerase is efficiently stopped when reaching the next hybridized random primer allowing only the fragment closest to the 3′ end being captured for later indexed adapter ligation and PCR amplification. The processed libraries were assessed for their size distribution and concentration using the BioAnalyzer High Sensitivity DNA Kit (Agilent Technologies). The libraries were pooled and diluted to 3 nM using 10 mM Tris-HCl, pH 8.5, and then denatured using the Illumina protocol. The denatured libraries were loaded onto an S1 flow cell on an Illumina NovaSeq 6000 (Illumina) and run for 53–101 cycles according to the manufacturer's instructions. After the quality and polyA trimming by BBDuk and alignment by HISAT2 (version 2.1.0) (Kim et al., 2015), read counts were calculated using HTSeq (Anders et al., 2015) by supplementing Ensembl gene annotation (GRCm38.78). DESeq2 R package (Love et al., 2014) was used to determine differentially expressed genes by taking into account a paired design where each mouse individual was compared between ipsilateral and contralateral. Specifically, we used a multi-factor design which included the information for each individual mouse as a term in the design formula. This accounted for differences between the samples (mouse individuals in our design) while estimating the effect due to the condition (treatment, or site difference [i.e., ipsilateral or contralateral OB]) in our design.

Differentially expressed genes were defined to be those with adjusted p-value < 0.1 calculated by the Benjamini-Hochberg method to control the false discovery rate (FDR). The ggplot2 R package (Wickham, 2016) was used for generating a heatmap. The list of differentially expressed genes was subjected to Core Analysis offered by Ingenuity Pathway Analysis (IPA). IPA Core Analysis offers multiple analyses including Pathway Analysis which predicts pathways that are changing based on gene expression and Upstream Regulator Analysis which predicts what regulators caused changes in gene expression, directional state of the regulator, and creates de novo pathways based on upstream regulators (Mechanistic Networks).

Fastq files and raw read counts generated during this study are available at GEO (GSE185945).

2.3. Immunostaining

Olfactory tissues were coronally cut on a cryostat into 20 μm slices, mounted on slide glasses, dried and stored at −80 °C until use. The sections were rehydrated with TBST (10 mmol/L Tris-HCl [pH 7.4] and 100 mmol/L NaCl with 0.3% Triton-X100 [vol/vol]), blocked with blocking buffer (5% normal donkey serum [vol/vol] in TBST) at room temperature for 1 h, and incubated with primary antibodies diluted in blocking buffer overnight at 4 °C. The antibodies and dilutions used in the present study are as follows: mouse anti-Ankyrin G IgG2a (NeuroMab, catalog #75–146, 1:500), chicken anti-green fluorescent protein (GFP; Abcam, catalog #ab13970, 1:1000) which also recognizes YFP, mouse anti-Calretinin (NeuroMarkers, catalog #MA5-14540, 1:400), Alexa Fluoro 488 mouse anti-Tbx21 (Biolegend, catalog #644830, 1:300), rabbit anti-Phospho-S6 Ribosomal Protein (PS6; Cell Signaling Technology, catalog #4854S, 1:1000), rabbit anti-Parvalbumin (Millipore Sigma, catalog #MAB1572, 1:300), and rabbit anti-Somatostatin (ImmunoStar, catalog #20067, 1:300). For double immunostaining with fluorescence, Alexa Fluoro 488-conjugated or 555-conjugated donkey antispecies IgGs (Thermo Fisher Scientific) were used as secondary antibodies (1:300) and incubated on tissue sections at room temperature for 1 h. Nuclei were counterstained with 4',6-diamidino-2-phenylindole (DAPI). The sections were coverslipped with fluorescence mounting medium (Dako Agilent) and imaged using the Zeiss Axio Imager M2 fluorescent microscope with an automated motorized XY stage. All images were acquired using the same excitation light intensity, exposure time, and numerical aperture of the objective lens.

2.4. Image analyses and morphometry

Five OB sections were stained from each mouse brain with calretinin and DAPI and divided into each OB sublayer (including the superficial and deep EPL) to measure their area. Cells that were positive for DAPI, Tbx21, and YFP in the MCL and EPL were defined as MCs and TCs, respectively, and were subsequently counted to determine the numbers in their respective layers. The area of the superficial and deep (s/d)EPL were measured separately by using Photoshop software. The lengths of YFP-positive (YFP+) dendrites were measured in the sEPL and dEPL separately by manual tracing in the FIJI/ImageJ software using the ROI Manager tool with the freehand line tracer. The primary method of normalizing the dendrite data was to divide the total length of dendrites per OB (in μm) by the number of YFP + somata in that OB (final units in μm/cell). Similarly, we also normalized this data with respect to dendrite density by converting the sEPL and dEPL areas to square millimeters (mm^2) and divided the total length of dendrites (in μm) in each layer of each OB section by the respective area in mm^2 (resulting units of μm/mm^2). Axon initial segments (AISes) were measured in a region defined by a rectangle with an area of 650 × 450 μm^2 in both the medial and lateral portion of the OB. AISes were defined by positive Ankyrin G staining and all AISes in the region were counted and measured in length (μm) and were analyzed via manual tracing in the FIJI/ImageJ software using the ROI Manager tool with the freehand line tracer.

2.5. Experimental design and statistical analysis

Comparisons of the relative OB sizes and AIS length/count among contralateral and ipsilateral OBs were statistically analyzed by one-way analysis of variance followed by Tukey's HSD post-hoc tests for multiple comparisons. Comparisons of dendrite length among contralateral and ipsilateral OBs were statistically analyzed by paired t-tests due to differences in inherent cre-recombination and subsequent expression of YFP. A p-value ≤ 0.05 indicated a significant difference. Statistical analyses were performed using Prism software (GraphPad Software, Inc.). Values are reported as means ± SEM.

3. Results

3.1. Upregulation of interferon-γ-driven inflammatory pathways following 4-week COI

We first aimed to examine gene expression signatures affected by early-stage COI. To induce COI, LPS administrations took place three times per week for 4 weeks and were carried out unilaterally to the left naris of each mouse, with the right serving as an internal control. The OB ipsilateral to the side of the injected naris is referred to as *ipsilateral* (*ipsi*), and the opposite OB (control) as *contralateral* (*contra*). Differential gene expression analysis was performed between the ipsilateral and contralateral OB from mice administered LPS (i.n., unilateral; n = 3) for 4 weeks. We identified 47 genes upregulated and 18 downregulated in the ipsilateral OBs compared to contralateral OBs (p-value < 0.1; Fig. 1A). To understand the functional relevance of these clusters, we performed functional annotation analysis for these 65 genes using Ingenuity Pathway Analysis (IPA, Qiagen). The Core Analysis highlighted the most significantly enriched and activated Canonical Pathway as "Neuroinflammation Signaling Pathway" (-log(p-value) = 5.95, z-score = 2.646, Fig. 1B). Molecules directly involved in this pathway include B2M, CCL5, CYBB, HLA-A, HLA-DQA1, HLA-DQB1, HLA-DRB5, and RAC2.

Next, we examined the upstream regulator in the IPA Core Analysis and identified 83 significant upstream regulators (z-score ≥ 2), with interferon-γ (IFN-γ) having the highest z-score (p-value = 5.04E-20, z-score = 4.749, Supplementary Table 1). Although the expression level of IFN-γ itself is not altered, the significant number of related downstream molecules including B2M, Bst2, C1QA, C1QB, C4A/C4B, CCL5, CD74, CTSS, Cxcl9, CYBB, GBP2, GFAP, HLA-A, HLA-DQA1, HLA-DQB1, HLA-

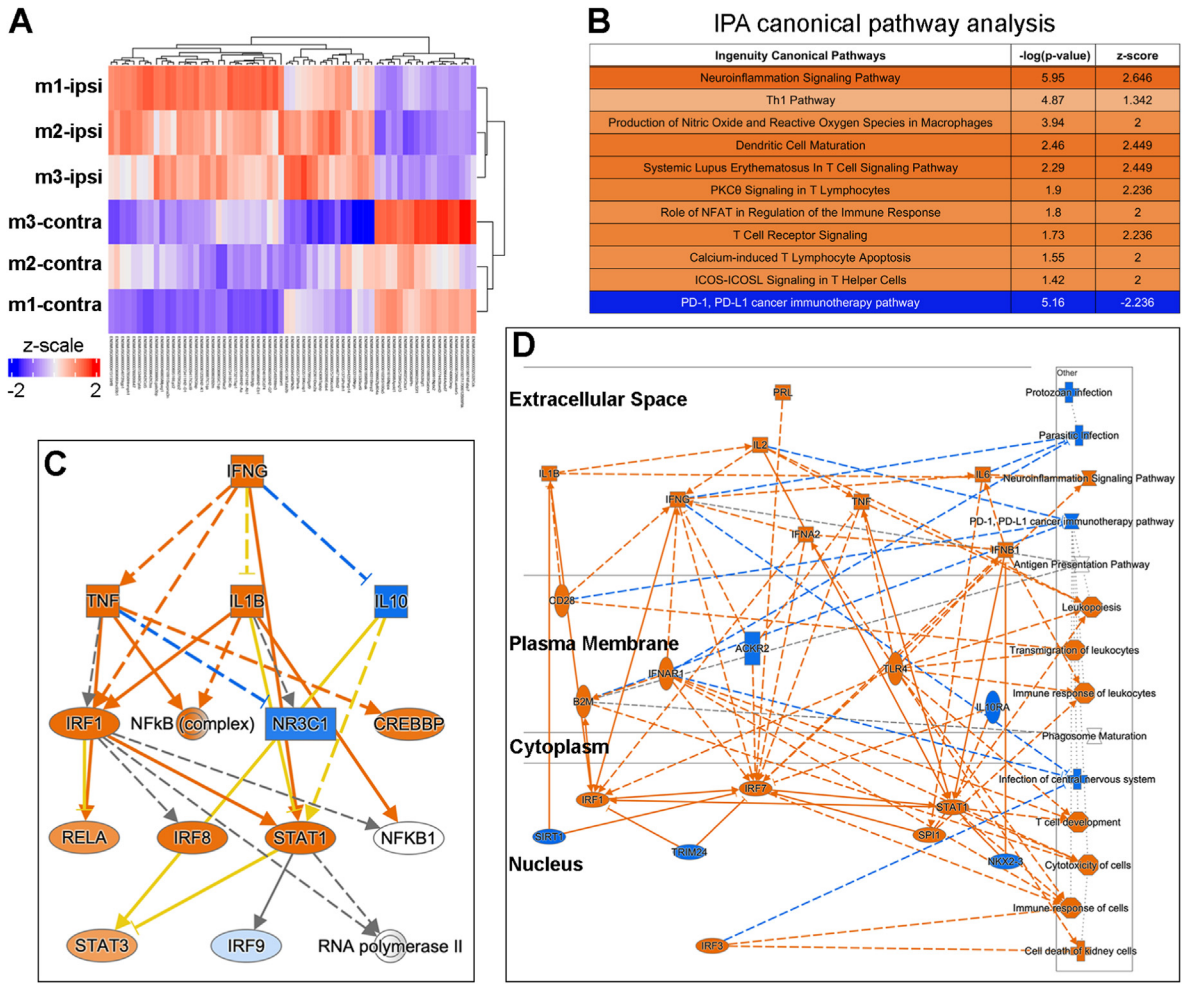

Fig. 1. Differentially expressed genes in the OB following 4-week COI.
(A) Heatmap of differentially expressed genes. **(B)** Most significant Canonical Pathways of differentially expressed genes. **(C)** Mechanistic Network of the most significantly activated Upstream Regulator, IFN-γ. **(D)** Graphical summary of differentially expressed genes illustrated with their subcellular localizations. Each entity has passed a fisher's exact test p-value cut-off of 0.05 and absolute z-score cut-off of 2 or greater. In panels (B–D), orange represents upregulated genes or activated pathways, where blue represents downregulated genes or inhibited pathways. Details for shapes of nodes and colors or patterns of lines can be found in the IPA's website (https://qiagen.secure.force.com/KnowledgeBase/articles/Basic_Technical_Q_A/Legend). (For interpretation of the references to color in this figure legend, the reader is referred to the Web version of this article.)

DRB5, Ifi47, IFITM3, Igtp, Iigp1, IRF1, IRF8, LGALS3BP, PARP14, PENK, RAC2, TAP1, and TAPBP are upregulated. The Mechanistic Network (Fig. 1C), a method to predict signaling cascades that connect other significantly represented upstream regulators to elicit the observed gene expression changes, demonstrated that IFN-γ may orchestrate with other cytokines such as TNF-α and IL-1β and regulate cascades of intracellular signaling to lead to activations of multiple transcription regulators such as IRF1, NF-kB complex, CREBBP, RELA, IRF8, STAT1, and STAT3. NR3C1, on the other hand, is downregulated and its inhibition is predicted to be mediated by TNF-α.

Finally, we summarize our findings by IPA's Graphical Summary (Fig. 1D) to provide an overview of the major biological themes in the IPA analysis by selecting the most significant entities identified in the Core Analysis such as Canonical Pathways, Upstream Regulators, and Disease and Biological Functions, further representing how they relate to each other. The Graphical Summary demonstrates how upregulated/activated (shown in orange) and downregulated/inhibited (shown in blue) genes, pathways, or diseases interact with each other. In addition to the activation of Neuroinflammation Signaling Pathway observed in the Canonical Pathway analysis (Fig. 1B) and IFN-γ which was depicted in the Upstream Regulator analysis (Fig. 1C), we revealed that many pathways associated with immune responses and leukocyte activities are activated, while infectious status is predicted to be inhibited.

3.2. Reduction of tufted cell lateral dendrites following 10-week COI

The presence of proinflammatory cytokines such as IFN-γ and TNF-α are capable of causing dendritic atrophy, retraction, and loss of synapses in primary neuronal cultures (Kim et al., 2002). It is important to note that LPS-induced COI does not cause the death of OB projection neurons (MCs/TCs) at any point up to the 24-week time point (Hasegawa-Ishii et al., 2017, 2019, 2020). Therefore, we aimed to explore the potential phenomenon of dendritic retraction of MCs/TCs following our COI paradigm.

In order to observe changes to the somata and dendritic morphology of MCs/TCs in the OB, we used Pcdh21-CreER x YFP (+/Het) transgenic mice unilaterally administered with LPS (i.n.) for 10 weeks. Protocadherin-21 (Pcdh21) is a member of the protocadherin homophilic cell-adhesion protein family uniquely expressed in MCs/TCs in the mouse OB (Nagai et al., 2005). On the final LPS-administration day, the mice were treated with tamoxifen (i.p., 30 mg/kg) to activate CreER for the YFP expression from the ROSA site and sacrificed 3 days after the injection.

As expected, the overall shape of the ipsilateral OB appears to be atrophied and narrower compared to the contralateral OB (Fig. 2A). Cell bodies and dendrites expressing YFP were observed in the GL, EPL, and MCL of both OBs (Fig. 2B and C). There were no differences in the total number of TCs, YFP + cells in the EPL, counted from 5 coronal OB sections (contra., 72.00 ± 17.58 vs ipsi., 72.67 ± 21.39). The number of MCs, YFP + cells in the MCL, was smaller than that of TCs but not significantly different comparing the contralateral to the ipsilateral OBs (contra., 23.67 ± 12.86 vs ipsi., 29.00 ± 16.92). This data suggests that the +/Het transgenic model preferentially labels TCs over MCs in the OB, and LPS treatment does not influence the expression of YFP in OB projection neurons.

Next, we analyzed the YFP + dendrites in the EPL. In the contralateral OB, the total length of YFP + dendrites counted from 5 coronal sections was significantly greater in the sEPL than in the dEPL (Fig. 2B; 15217 ± 1332 μm vs 7421 ± 1905 μm, respectively; $p = 0.0014$). However, the length of YFP + dendrites in the ipsilateral OB was not statistically different between sEPL and dEPL (Fig. 2C; 10095 ± 1470 μm vs 7327 ± 1588 μm, respectively; $p = 0.2210$). The total length of YFP + dendrites in the sEPL was significantly reduced in the ipsilateral OB compared to that of contralateral OBs ($p = 0.0178$). However, the densities of YFP + dendrites were not significantly different in the sEPL ($p = 0.7458$) nor in the dEPL ($p = 0.9751$) between contralateral and ipsilateral OBs, which is consistent with the area reduction of the sEPL but not dEPL in the ipsilateral OB (Hasegawa-Ishii et al., 2019, 2020).

In order to normalize the effects of COI on the dendrites of MCs and TCs, we calculated ratios of YFP + dendrites (length in μm) to YFP + cell bodies measured in each OB (μm/cell). This allows us to normalize for variability in our data that may exist due to animal differences in CreER expression. Upon analysis, we observed a significant reduction of dendrites in the sEPL (Fig. 2D; contra., 223.1 ± 74.70 μm/cell vs ipsi., 152.4 ± 69.77 μm/cell; $p = 0.0073$). However, we did not observe any changes to dendrite density in the dEPL (Fig. 2E; contra., 382.5 ± 190.6 μm/cell vs ipsi., 345.2 ± 244.4 μm/cell; $p = 0.3594$). These results suggest that the overall length of TC, but not MC, dendrites has been reduced.

3.3. Alterations in the axon initial segment of tufted cells following 10-week COI

Our findings of decreased TC dendrites have led us to believe that there may be further physiological impairments to TCs following COI. The axon initial segment (AIS) is the site of a neuron that separates its somatodendritic and axonal compartments, and is primarily responsible for maintaining the neuron's polarity and initiating action potentials (Ogawa and Rasband, 2008). One of the most essential components of the AIS is the cytoskeletal-associated protein, Ankyrin-G (AnkG) (Alshammari et al., 2016). Previous studies have shown that shorter or fewer AISes measured by AnkG are indicative of impairments to the neuron's physiology, such as a decrease in excitability (Ogawa and Rasband, 2008; Galliano et al., 2021; Yamada and Kuba, 2016). We first co-stained OB sections with AnkG and Tbx21, an OB projection neuron-pecific marker, and confirmed that the vast majority of AnkG + AISes present in the EPL and MCL are derived from TCs and MCs, respectively. (Supplementary Fig. 1).

We then measured the length of each individual AIS, as well as the number in each OB. Since our previous studies primarily investigated the response of LPS-treatment on the medial and lateral OBs, we chose to focus on these regions as well. Through this analysis, we observed a significant reduction in the number of AISes in the ipsilateral OB EPL (Fig. 3A and B). Our data demonstrated that fewer AISes were present in the lateral EPL of the ipsilateral OB. The number of AISes in the lateral OB EPL decreased from 165.6 ± 47.45 AISes in the contralateral OB to 94.20 ± 29.24 in the ipsilateral OB (Fig. 3F histogram; $p = 0.0175$). This phenomenon, however, was not found in the medial OB EPL (Fig. 3E histogram; contra., 165.4 ± 26.47 vs ipsi., 130.8 ± 24.81; $p = 0.3829$).

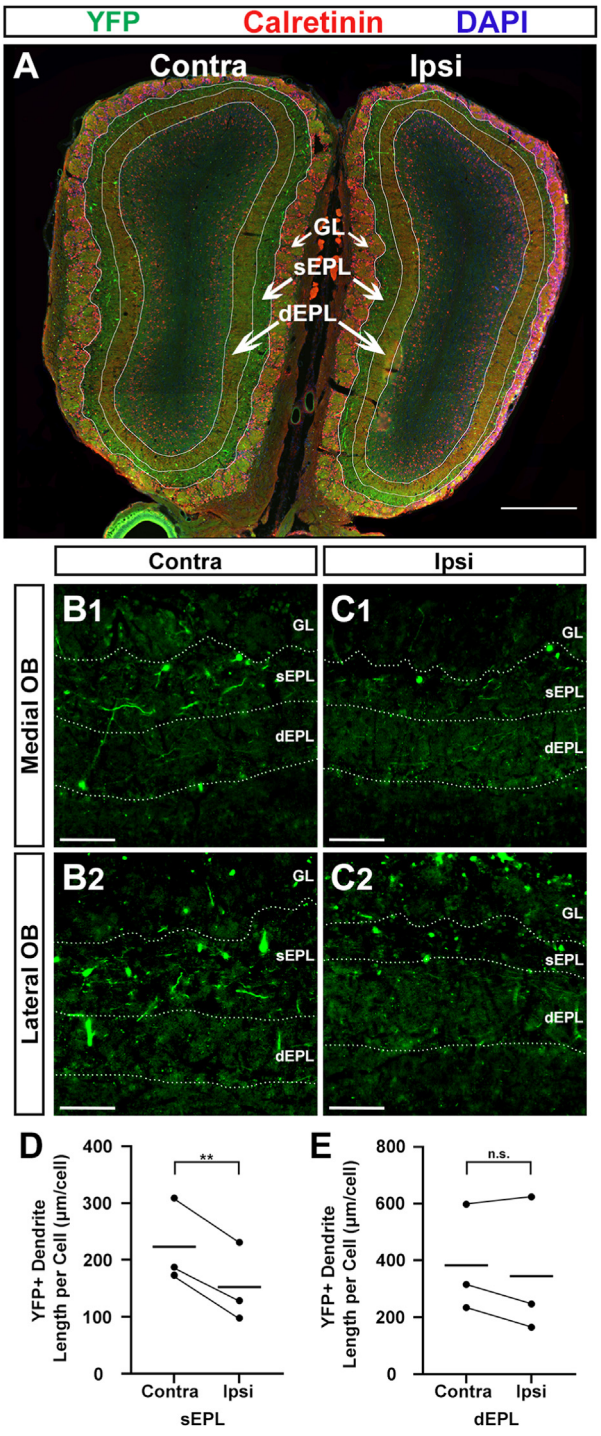

Fig. 2. Reduction of tufted cell lateral dendrites following 10-week COI. **(A)** Coronal section of the OBs stained for YFP, calretinin, and DAPI. Calretinin is used to delineate between the superficial and deep EPL, where the lateral dendrites of TCs and MCs exist, respectively. **(B)** Enlarged view of the medial (B1) and lateral (B2) contralateral OB. **(C)** Enlarged view of the medial (C1) and lateral (C2) ipsilateral OB. The Pcdh21-CreER x YFP transgenic mouse model (+/Het) preferentially labels TCs and their lateral dendrites compared to MCs. **(D, E)** Graphs show the densities of lateral dendrites for TCs (D) and MCs (E) in μm of dendrites per cell. Dendrite densities of TC lateral dendrites decreased significantly in the ipsilateral OB compared to contralateral. There were no changes in the densities of MC lateral dendrites. Individual data are plotted, and the means are shown as bars. Data in D and E were analyzed with a paired *t*-test: **$p < 0.01$ compared to contralateral OB (control). Scale bars, 500 μm (A), and 100 μm (B, C).

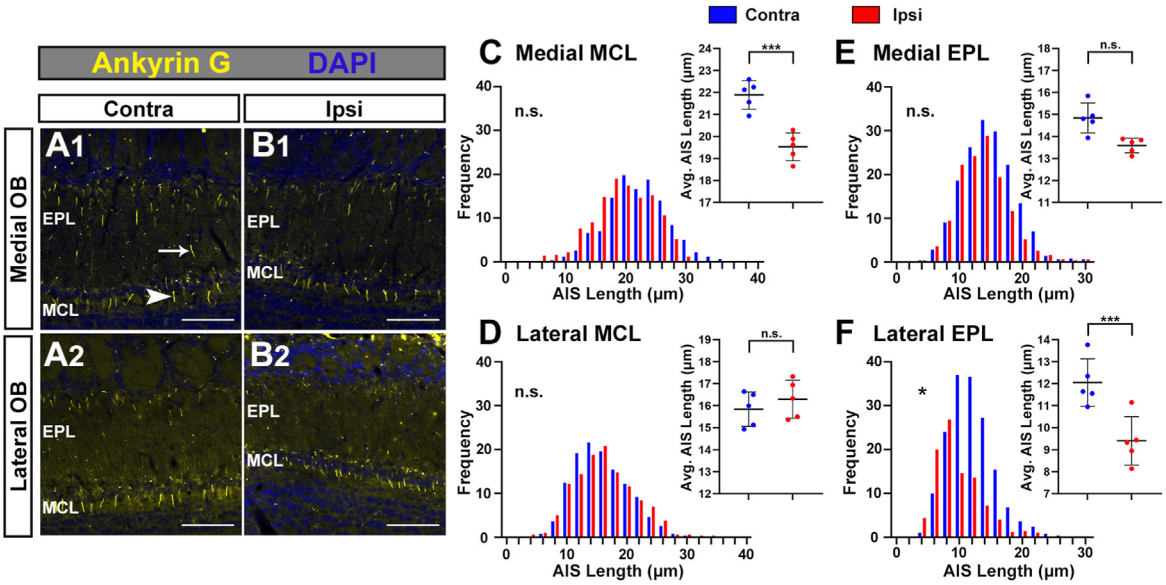

Fig. 3. Reduction and shortening of tufted cell axon initial segments following 10-week COI.
(A, B) Coronal sections of the OBs stained for Ankyrin G and DAPI. Axon initial segments of TCs and MCs exist in the EPL and MCL, respectively. (A) Enlarged views of the medial (A1) and lateral (A2) contralateral OB. (B) Enlarged views of the medial (B1) and lateral (B2) contralateral OB. **(C–F)** Histograms show the frequency of axon initial segments at various lengths from five coronal OB sections for each mouse (n = 5). Graphs show differences in the average length of AIS length comparing the contralateral to ipsilateral OB. Data are shown as mean ± SEM. There were no differences in the number of MC AISes counted in either the medial (C, histogram) or lateral (D, histogram) OBs. MC AISes in the medial OB appeared to have shortened in length (C, graph), whereas those in the lateral OB did not change in length (D, graph). There were no differences in the number of TC AISes counted in the medial OB (E, histogram). The TC AISes in the lateral OB were the only AISes to significantly decrease in number (F, histogram). TC AISes in the medial OB did not change in length (E, graph), whereas those in the lateral OB significantly decreased (F, graph). Data in C–F were analyzed by one-way analysis of variance followed by Tukey's HSD post-hoc tests for multiple comparisons: *$p < 0.05$, ***$p < 0.001$ compared to contralateral OB (control). Scale bars, 100 μm.

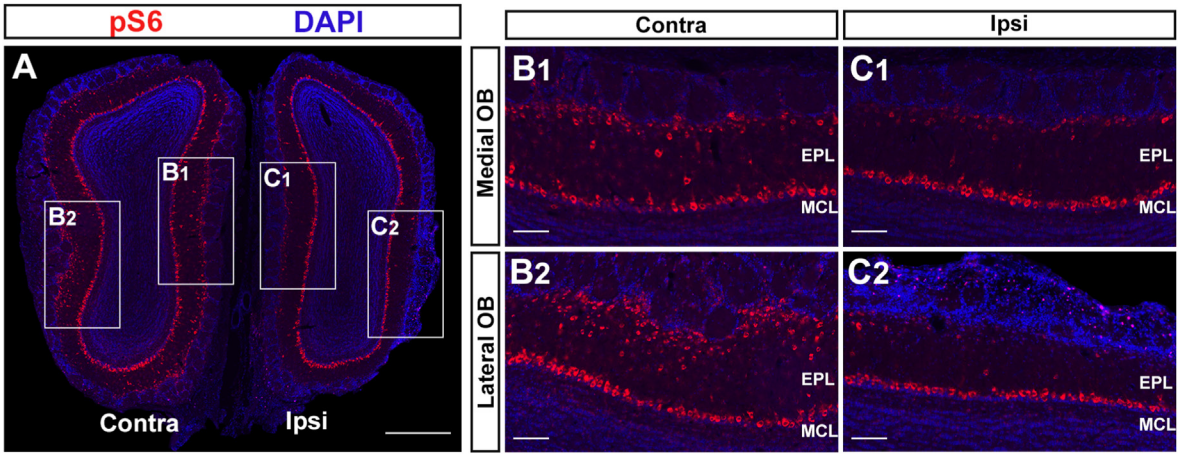

Fig. 4. Reduced cellular activity of the OB following 10-week COI.
(A) Coronal sections of the OB stained with pS6 and DAPI. TCs express less pS6 in the ipsilateral OB compared to the contralateral OB following 10-week COI, whereas MCs are unaffected. **(B)** Enlarged view of the medial (B1) and lateral (B2) contralateral OB. **(C)** Enlarged view of the medial (C1) and lateral (C2) ipsilateral OB. Scale bars, 500 μm (A), and 100 μm (B, C).

For both OBs, there were no differences in the number of MCL AISes counted, regardless of laterality (Fig. 3C and D histograms; medial contra., 119.2 ± 12.76; lateral contra., 122.6 ± 23.09; medial ipsi., 120.2 ± 16.25; lateral ipsi., 120.6 ± 24.17).

We further analyzed the length of the AISes that were present in each OB. Since TCs reside solely in the EPL and MCs in the MCL, we have classified the AISes measured in the EPL as belonging primarily to TCs and AISes in the MCL as those of MCs. It was determined that the TC AISes in the lateral OB significantly decreased in their length (Fig. 3F; contra., 12.05 ± 1.079 μm vs ipsi., 9.399 ± 1.100 μm; $p = 0.0009$). This phenomenon was not found for the TC AISes in the medial OB (Fig. 3E; contra., 14.84 ± 0.6815 μm vs ipsi., 13.58 ± 0.3369 μm; $p = 0.1370$). Although there was no change in the number of MC AISes in the medial OB, it did appear that the AISes present in the medial region of the OB significantly decreased in length (Fig. 3C; contra., 21.88 ± 4.978 μm vs ipsi., 19.49 ± 4.964 μm; $p = 0.0006$). However, the length of MC AISes in the lateral OB did not appear to shorten (Fig. 3D; contra., 15.84 ± 0.7814 μm vs ipsi., 16.29 ± 0.8635 μm; $p = 0.7684$). Collectively, these results suggest that COI has the most significant effect on TCs morphologically and physiologically in the lateral OB.

3.4. Reduction in tufted cell activity following 10-week COI

To examine the alterations in cellular activity of the OB projection neuros, we stained OBs with an antibody against phospho-S6 ribosomal protein (pS6), one of many neuronal activity markers (Knight et al.,

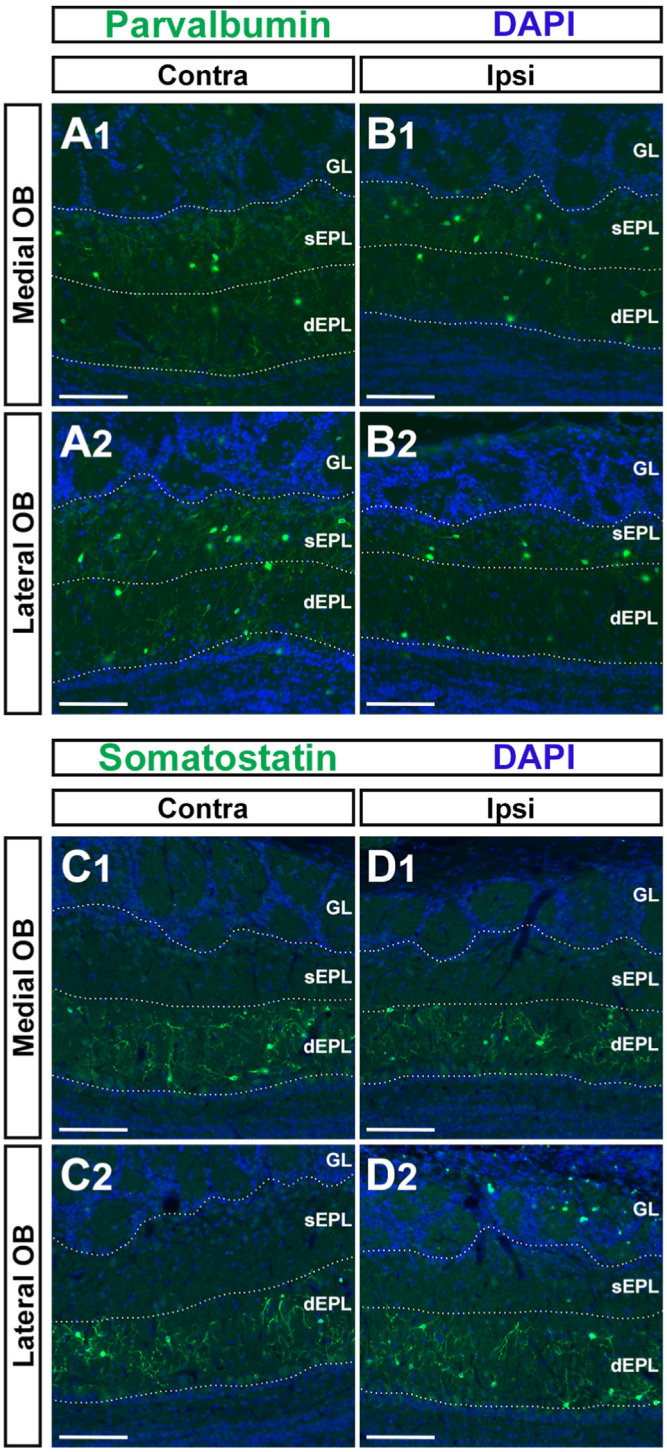

Fig. 5. No changes in the number of OB interneurons following 10-week COI. **(A, B)** Coronal sections of the OBs stained for parvalbumin (PV) and DAPI. More PV + interneurons exist in the sEPL than in the dEPL of the untreated OB. However, the number of PV + interneurons in each EPL sublayer of the ipsilateral OB was not significantly different from that of the contralateral OB. **(C, D)** Coronal sections of the OBs stained for somatostatin (SST) and DAPI. There were no differences in the number of SST + interneurons in the dEPL between the contralateral and ipsilateral OBs. Data in A-D were analyzed by one-way analysis of variance followed by Tukey's HSD post-hoc tests for multiple comparisons. Scale bars, 100 μm.

2012). A recent study demonstrated that pS6 is an exceptional activity marker for OB projection neurons, and that naris occlusion is capable of significantly reducing the expression of pS6 among projection neurons on the ipsilateral OB (Galliano et al., 2021). It is also worth noting that the vast majority of pS6-expressing projection neuron somata were double-positive for Tbx21 (Supplementary Fig. 2). Upon immunohistochemical analysis of mice that underwent the 10-week unilateral COI paradigm, we observed robust pS6 staining throughout the entire MCL and EPL of the contralateral OB (Fig. 4). In contrast, we observed fewer pS6-positive projection neuron somata throughout the EPL in the ipsilateral OB. The MCL, however, did not appear to have any reduction in pS6 signal (Fig. 4B and C). These findings further suggest that functional impairments may be occurring to TCs rather than MCs throughout the ipsilateral OB.

3.5. No apparent loss of OB interneurons following 10-week COI

Olfactory information is not only processed by OB projection neurons but requires substantial communication with a variety of OB interneurons. Based on their location in the OB, interneurons play a major role in fine-tuning of olfactory information before it even reaches the cortex. OB interneurons can also be further differentiated by their immunoreactivity (Nagayama et al., 2014). For example, the parvalbumin-positive (PV+) and somatostatin-positive (SST+) interneurons are found in the EPL and are distributed primarily throughout the sEPL and dEPL, respectively (Nagayama et al., 2014; Liu et al., 2019; Miyamichi et al., 2013; Lepousez et al., 2010a). Here, we investigated whether the effects of COI on TCs would extend to interneurons residing throughout the sEPL and dEPL. Fig. 5 shows PV+ and SST + interneurons in the sEPL and dEPL of the contralateral and ipsilateral OBs following the 10-week COI paradigm. To quantify the effects of COI on these interneurons, we counted the numbers from 5 coronal sections (n = 5 mice). Consistent with previous literature, there were more PV + interneurons in the sEPL than in the dEPL of the contralateral OB (333.0 ± 29.04 vs 256.0 ± 30.55, respectively; p = 0.0037) (Anders et al., 2015). However, the number of PV + interneurons in each EPL sublayer of the ipsilateral OB was not significantly different from that of the contralateral OB (Fig. 5A and B; sEPL: contra., 333.0 ± 29.04 vs ipsi., 298.8 ± 33.91, p = 0.2874; dEPL: contra., 274.0 ± 22.15 vs ipsi., 256.0 ± 30.55, p = 0.7660). Similarly, as SST + interneurons are not present in the sEPL (Lepousez et al., 2010b), we counted only from the dEPL. No differences were observed in the number of SST + interneurons following 10-week COI (Fig. 5C and D; contra., 167.4 ± 16.83 vs ipsi., 169.4 ± 12.64; p = 0.3859). Collectively, this data suggests that there is no change in the number of PV + or SST + interneurons in the OB following the 10-week COI paradigm.

3.6. Remodeling of tufted cell lateral dendrites after recovery period following 10-week COI

Our previous studies demonstrated that a 10-week period of no LPS treatment following the 10-week COI paradigm resulted in a recovery of the OB atrophy and depletion of inflammatory responses (Hasegawa-Ishii et al., 2020). Therefore, we sought to investigate if the recovery phenomenon would extend to the OB on a cellular level. For this experiment, we used male +/Het mice (n = 3) treated with LPS for 10 weeks followed by a 10-week recover period of no treatment. We first investigated if TC lateral dendrites recover from their reduction caused by COI.

Consistent with our previous studies, the overall shape of the ipsilateral OB appears to undergo a complete recovery (Hasegawa-Ishii et al., 2019, 2020). We counted the total number of YFP + cells in the EPL of the contralateral and ipsilateral OBs and observed more YFP + TC soma in the ipsilateral OB compared to the contralateral (contra., 64.00 ± 15.52 vs ipsi., 79.00 ± 14.42; p = 0.0131). The number of YFP + MCs, however, was not significantly different (contra., 16.00 ± 6.083 vs ipsi., 17.33 ± 1.528; p = 0.6667). To compensate the difference in the numbers of labeled YFP + cells, the total number of YFP + dendrites in the sEPL and dEPL were divided by the total number of YFP + TCs and MCs, respectively. Surprisingly, even after this normalization, we still

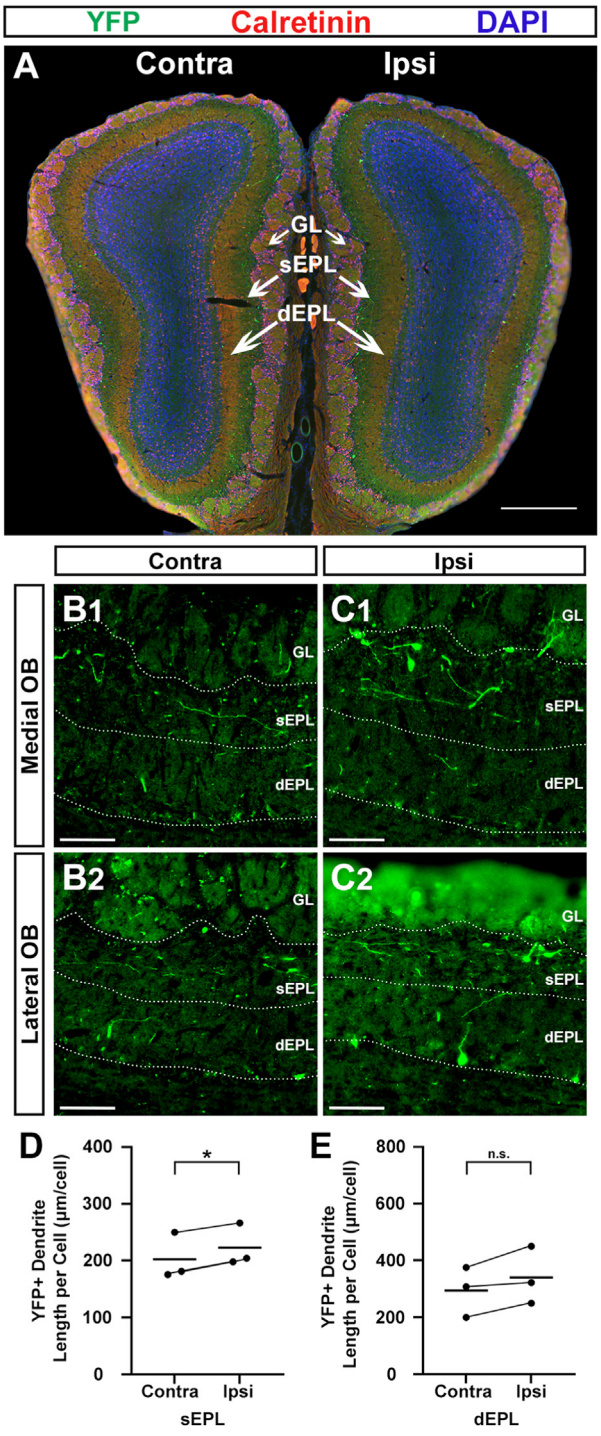

Fig. 6. 10-week recovery period restores tufted cell lateral dendrites following 10-week COI.

(A) Coronal section of the OBs stained for YFP, calretinin, and DAPI. Calretinin is used to delineate between the superficial and deep EPL, where the lateral dendrites of TCs and MCs exist, respectively. **(B)** Enlarged view of the medial (B1) and lateral (B2) contralateral OB. **(C)** Enlarged view of the medial (C1) and lateral (C2) ipsilateral OB. **(D, E)** Graphs show the densities of lateral dendrites for TCs (D) and MCs (E) in μm of dendrites per cell. Dendrite densities of TC lateral dendrites were greater in the ipsilateral OB compared to contralateral. There were no changes in the densities of MC lateral dendrites. Individual data are plotted, and the means are shown as bars. Data in D and E were analyzed with a paired *t*-test: *$p < 0.05$ compared to contralateral OB (control). Scale bars, 500 μm (A), and 100 μm (B, C).

observed a slightly significant increase of dendrites in the ipsilateral sEPL compared to contralateral (Fig. 6D; contra., 202.1 ± 41.38 μm/cell vs ipsi., 222.8 ± 37.70 μm/cell; $p = 0.0357$). We did not observe any changes to dendrite length in the dEPL (Fig. 6E; contra., 294.0 ± 88.64 μm/cell vs ipsi., 340.6 ± 101.2 μm/cell; $p = 0.1139$). Thus, our results suggest that the overall length of TC dendrites has not only recovered, but the TCs may have more dendrites in the ipsilateral OB following the 10-week recovery period.

3.7. Stabilization of tufted cell activity and axon initial segment integrity after recovery period following 10-week COI

Lastly, we investigated the effect of a recovery period on the integrity of the AIS of MCs and TCs following COI. We performed the same analysis as previously stated and observed no significant differences between the ipsilateral and contralateral OBs in either the length or number of AISes for both MCs and TCs (Fig. 7). These results indicate that no apparent "over-recovery" phenomenon occurs with respect to TC AIS integrity. Combined with our previous findings, these results suggest that the TC AISes in the lateral OB that are damaged following COI are capable of returning back to appropriate lengths, essentially re-stabilizing, allowing for a restoration in the transfer of OB information. Consistent with this observation, there was no apparent reduction of the pS6 expression in the EPL of the ipsilateral OB in mice who underwent the 10-week COI paradigm followed by a 10-week recovery period of no treatment (Fig. 8). These results suggest that a functional recovery of TCs occurs after a sufficient period without exposure to LPS.

4. Discussion

In this study, we found that COI induced by i.n. administration of LPS causes dendritic retraction and axonal instability of TCs, but not MCs, in the mouse OB. The superficial OB layers (GL, ONL, sEPL) are the primary region of OB atrophy and inflammation at 10 weeks of LPS administrations (Hasegawa-Ishii et al., 2019, 2020). Our results suggest that the reduction of dendrites that was observed in the ipsilateral OB is primarily attributed to a reduction in the sEPL. Similarly, the shortening and loss of AISes takes place primarily in the lateral EPL of the ipsilateral OB, a region that has been proven to be most susceptible to COI at this time point.

The signaling cascades downstream of proinflammatory cytokines such as IFN-γ and TNF-α has been demonstrated to occur in the OB as early as at 4 weeks of i.n. LPS administrations. These cytokines are capable of inducing the retraction of neuronal dendrites and synaptic degradation in primary neuronal cultures (Kim et al., 2002). We anticipate that a similar phenomenon is taking place in our current paradigm in which the presence of proinflammatory cytokines and activated glial cells among the superficial OB layers induce neuronal stress and subsequent structural dysregulation. An interesting finding is that NR3C1, the glucocorticoid receptor, was downregulated in the OB at 4 weeks of i.n. LPS administrations. NR3C1 has an overall anti-inflammatory influence by upregulating the expression of anti-inflammatory proteins in the nucleus while simultaneously downregulating the expression of pro-inflammatory proteins in the cytosol (Rhen and Cidlowski, 2005; Lu et al., 2006). Downregulation of NR3C1 in the OB during COI, therefore, may enhance the inflammatory responses.

Our previous study, however, demonstrated that cessation of COI results in a reduction of immune responses in the OB. This suggests that anti-inflammatory mechanisms may take place following the absence of persistent inflammation. Microglia and astrocytes are well established to engage in both pro- and anti-inflammatory activities (Pozzo et al., 2019; Shinozaki et al., 2017; Becerra-Calixto and Cardona-Gómez, 2017). The research from our lab thus far has established that cytokines such as TNF-α, IFN-γ, IL-1β, and IL-10 are significantly upregulated in the OB following COI. Although the former three are pro-inflammatory, IL-10 is

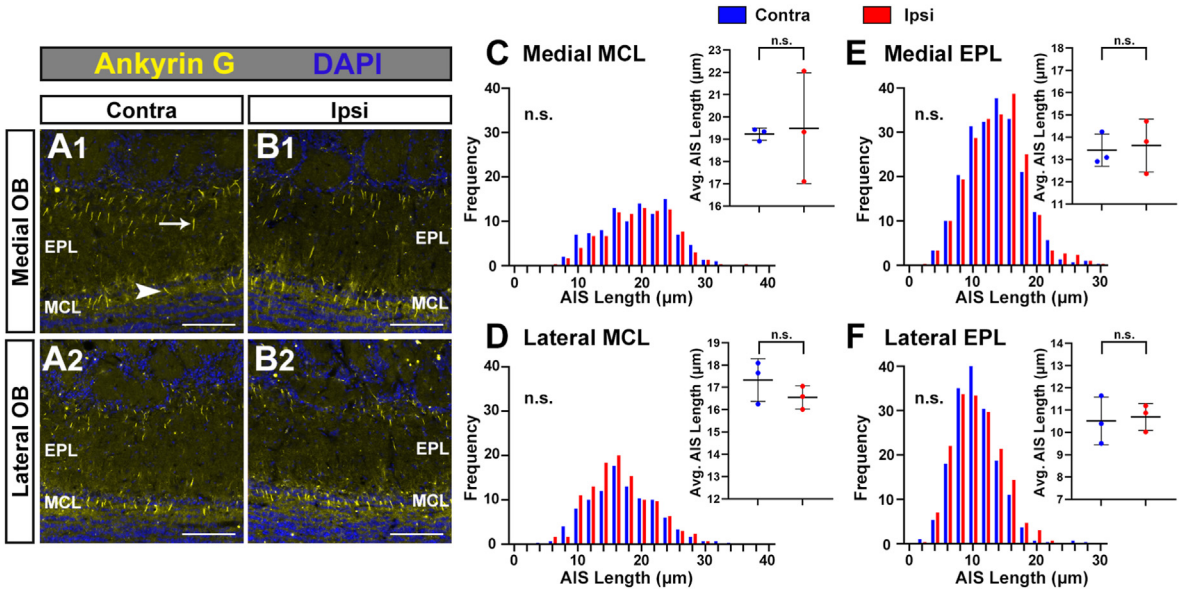

Fig. 7. 10-week recovery period restores tufted cell axon initial segments following 10-week COI.
(A, B) Coronal sections of the OBs stained for Ankyrin G and DAPI. Axon initial segments of TCs and MCs exist in the EPL and MCL, respectively. (A) Enlarged views of the medial (A1) and lateral (A2) contralateral OB. (B) Enlarged views of the medial (B1) and lateral (B2) contralateral OB. **(C–F)** Histograms show the frequency of axon initial segments at various lengths from five coronal OB sections for each mouse (n = 5). Graphs show differences in the average length of AIS length comparing the contralateral to ipsilateral OB. Data are shown as mean ± SEM. There were no differences in the number of MC AISes counted in either the medial (C, histogram) or lateral (D, histogram) OBs. No differences were observed in the lengths of MC AISes in either the medial (C, graph) nor lateral (D, graph) OBs. There were also no differences in the number of TC AISes counted in medial (E, histogram) or lateral (F, histogram) OBs. TC AISes in the medial OB did not change in length (E, graph) nor did those in the lateral OB (F, graph). Data in C–F were analyzed by one-way analysis of variance followed by Tukey's HSD post-hoc tests for multiple comparisons. Scale bars, 100 μm.

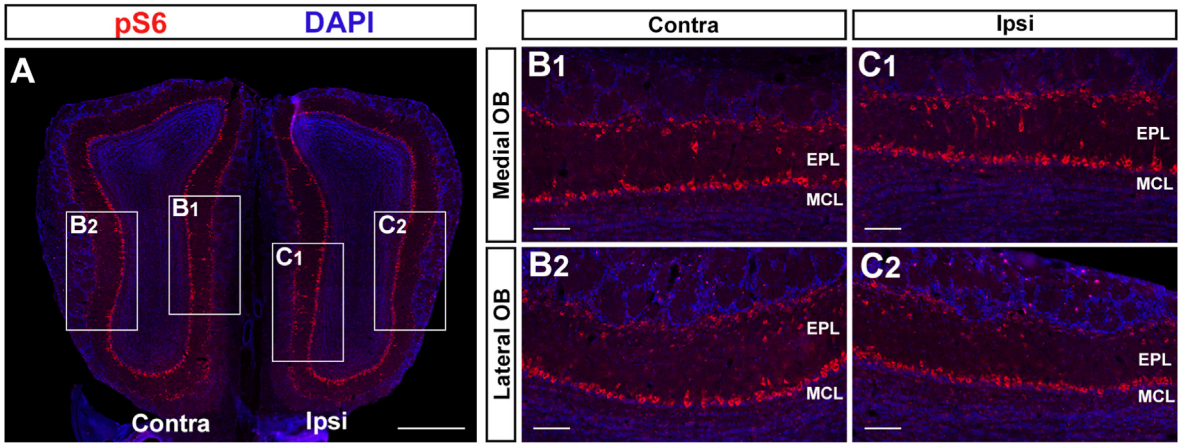

Fig. 8. 10-week recovery period restores cellular activity of the OB following 10-week COI.
(A) Coronal sections of the OB stained with pS6 and DAPI. The expression of pS6 among TCs has recovered in the ipsilateral OB after the 10-week recovery period following 10-week COI. **(B)** Enlarged view of the medial (B1) and lateral (B2) contralateral OB. **(C)** Enlarged view of the medial (C1) and lateral (C2) ipsilateral OB. Scale bars, 500 μm (A), and 100 μm (B, C).

an anti-inflammatory cytokine released by astrocytes which may act to maintain (or restore) neuronal homeostasis (Mizuno et al., 1994; Rasley et al., 2006). Interestingly, it is suggested that IL-10 provides neuroprotection and promotes neurite outgrowth and synapse formation (Chen et al., 2016). It was also shown that IL-10 restores the ability of synaptic plasticity among neurons after LPS-induced systemic inflammation (Lenz et al., 2020). The release of IL-10 and other neuroprotective agents may be a necessary step in evading, or recovering from, TC degeneration. Similarly, astrocytes and microglia are capable of mediating and amplifying axonal and dendrite growth through mechanisms including the release of fibroblast growth factor (FGF) and purinergic signaling, respectively (Le and Esquenazi, 2002; Chen et al., 2019; Eyo et al., 2015, 2021). The present study demonstrating a recovery effect of the observed TC dendritic retraction may be attributed to similar neuroprotective mechanisms via glial cell activity.

Our findings of reduced TC AIS number and length is highly suggestive of functional impairments to TC-integrated neural circuits. AISes are responsible for action potential initiation and maintenance of neuronal polarity (Ogawa and Rasband, 2008; Hedstrom et al., 2008). The actual assembly of the AIS is coordinated primarily by AnkG, a cytoskeletal-associated protein (Alshammari et al., 2016; Jenkins and Bennett, 2001). It remains unknown whether the mechanisms of AIS maintenance and AIS assembly (or reassembly) as controlled by AnkG are related (Le Bras et al., 2014). However, we speculate that the ability of

TCs to reconstruct their AISes in the recovery period following COI is possibly also coordinated by AnkG-mediated mechanisms. Nonetheless, dysfunctional AISes induced by diminished AnkG integrity will likely contribute to a decrease in excitability and signal transmission to a neuron's downstream targets (Jacques et al., 2014). It is also interesting to note that AnkG is necessary to maintain the structural and functional segregation of a neurons axon from its dendrites (Sobotzik et al., 2009). These implications suggest a potential biological connection between axon destabilization and dendritic retraction in our COI paradigm.

All of our sensory systems are comprised of first-, second-, and third-order neurons which uniquely relay sensory information to the CNS at each level. Therefore, it is plausible to assert that damage to the neural components at any of these levels will impair sensory processing in the CNS. Multiple clinical studies reported cortical atrophy and altered brain activity in response to spinal cord injury (Aguilar et al., 2010; Curt et al., 2002; Karunakaran et al., 2018). Similarly, clinical studies investigating the role of diabetic retinopathy on CNS have found remapping and impairments of the primary visual cortex following disease onset (Ferreira et al., 2017a, 2017b; Murphy et al., 2016). This phenomenon, however, has yet to be thoroughly investigated with respect to the olfactory system. COI causes ablation to the first-order neurons of the olfactory system (OSNs), which can occur after only one day of i.n. LPS administration (Hasegawa-Ishii et al., 2017), and this phenotype will persist for the duration of COI. Our current findings which model CRS suggest that olfactory information processing and transmission at the level of the second-order neurons (specifically, TCs) may be disrupted due to structural and functional pathophysiology. While the olfactory second-order neurons (MCs/TCs) share a multitude of features, they differ in two distinct ways, anatomically; (1) somata location within the OB, and (2) neurite projection patterns. MCs project their axons to most structures within the OC, whereas TC axons are more localized to targets including the anterior olfactory nucleus, olfactory tubercle, and anterior piriform cortex (Igarashi et al., 2012; Orona et al., 1984; Chon et al., 2020; Mori and Sakano, 2011). When drawing comparisons to other sensory systems, this information leads us to speculate that the differences in axonal projection patterns of MCs and TCs may also be a component of the olfactory system impacted by the pathophysiological nature of COI. More specifically, the third-order neurons of the olfactory system residing in the TC-targeted OC regions may also be impacted by COI in the form of cortical atrophy or even immune responses. Further studies are needed to address whether these OC regions are also susceptible to the neuropathological effects of COI.

Although the mechanism by which TCs and MCs differ in their sensitivity to COI is unknown, our current and previous studies suggest that a loss of input from OSNs to the OB glomeruli is the primary cause of TC-integrated OB layer thinning and a decrease in the extension of TC neurites (Hasegawa-Ishii et al., 2020). Interestingly, it was shown that BDNF, a neurotrophic factor that facilitates dendritic stabilization during development, is reduced in the sEPL after naris closure (Biju et al., 2008). Thus, OSN input may be required to maintain TC synapses and dendrites by activating the BDNF pathway. In addition, some neuromodulatory centrifugal fibers are more densely distributed in the dEPL where the MC lateral dendrites preferentially extend, rather than in the sEPL (Matsutani and Yamamoto, 2008). It is therefore likely that centrifugal fibers targeting the dEPL contribute to the regulation of MC activity, whereas OSN input may have a greater influence on TCs (Nagayama et al., 2004; Burton and Urban, 2014; Egaña et al., 2005; Geramita and Urban, 2017; Gire et al., 2012; Griff et al., 2008; Cang and Isaacson, 2003). It is possible that MCs may be functionally protected from loss of OSN input due to continuous input from other brain regions. Whether the loss of OSN input is a result of naris occlusion (Hasegawa-Ishii et al., 2020) or COI, our data demonstrates that the biological consequences of decreased OSN activity predominately impact TCs over MCs.

5. Conclusions

In conclusion, the findings presented in this report demonstrate that TCs undergo significant neurite dysregulation following COI primarily in the forms of lateral dendrite retraction and AIS shortening, whereas MCs, as well as PV+ and SST + interneurons, are largely unaffected. Our study also suggests that the mechanisms underlying neurite dysregulation are induced through common pathways involving IFN-γ, a pro-inflammatory cytokine. Furthermore, the pathological responses of TCs to COI was shown to recover following a period without olfactory inflammation. In summary, this study provides a strong foundation for investigating the cellular and molecular mechanisms responsible for regulating the reversible changes occurring in TC-integrated OB neural circuits. However, this study focused on mechanisms of inflammation resulting from bacterial infections in the olfactory system. Viruses, such as COVID-19, are also capable of inducing COI (Lee et al., 2021; Miller and Bhattacharyya, 2022; Wang et al., 2021), but viral CRS was not investigated in this study. Even so, the present results may provide evidence for comparable mechanisms between bacterial and viral CRS (Liao et al., 2014; Meltzer and Hamilos, 2011; Xydakis et al., 2021). It should also be noted that the findings from this animal study may not be directly applicable to humans. Nevertheless, we have revealed some of the major consequences of inflammation on the homeostatic functioning of OB projection neurons, as well as unveiled a novel pathway of neuroinflammation from the periphery to the CNS. Our findings provide a strong foundation for a potential mechanism for the transmission of inflammation from the periphery to the CNS via the olfactory system, similar to the olfactory vector hypothesis of neurodegenerative diseases (Doty, 2008). Our data provides insight to clinical interventions and treatments for CRS that target some of the key players in this state of inflammation, including the contributing cytokines reveled in our study. Developing a deeper understanding of the biological mechanisms underlying CRS and the consequences of inflammation-induced hyposmia is a vital next step to the overarching goal of enhancing human health.

Ethics approval and consent to participate

All protocols were approved by, and all methods were performed in accordance with the guidelines of the Institutional Animal Care and Use Committee of Penn State College of Medicine.

Consent for publication

Not applicable.

Availability of data and material

The datasets analyzed during the current study are available from the corresponding author upon reasonable request.

Funding source

The present study was supported by NIH grant R01DC016307 (FI).

Authors contributions

B.J.L. and F.I. designed research; B.J.L., Y.I., and A.I. performed research; B.J.L., Y.K., and F.I. analyzed data; B.J.L., Y.K., and F.I. wrote the paper.

Acknowledgement

This work was supported by NIH grant R01DC016307 (F.I.). We thank Dr. Andras Hajnal for critical reading of this manuscript.

Abbreviations

AIS	axon initial segment
AnkG	Ankyrin G
CNS	central nervous system
COI	chronic olfactory inflammation
CRS	chronic rhinosinusitis
dEPL	deep external plexiform layer
EPL	external plexiform layer
GL	glomerular layer
i.n.	intranasal
IFN-γ	interferon-γ;
LPS	lipopolysaccharide;
MC	mitral cell
MCL	mitral cell layer
OB	olfactory bulb
OC	olfactory cortex
OE	olfactory epithelium
ONL	olfactory nerve layer
Pcdh21	protocadherin-21
pS6	phoso-S6 ribosomal protein
PV	parvalbumin
sEPL	superficial external plexiform layer
SST	somatostatin
TC	tufted cell
YFP	yellow fluorescent protein

Appendix A. Supplementary data

Supplementary data to this article can be found online at https://doi.org/10.1016/j.bbih.2022.100451.

References

Aguilar, J., Humanes-Valera, D., Alonso-Calviño, E., et al., 2010. Spinal cord injury immediately changes the state of the brain. J. Neurosci. : Off. J. Soc. Neurosci. 30 (22), 7528–7537. https://doi.org/10.1523/JNEUROSCI.0379-10.2010.

Ahmad, N., Zacharek, M.A., 2008. Allergic rhinitis and rhinosinusitis. Otolaryngol. Clin. 41 (2), 267–281. https://doi.org/10.1016/j.otc.2007.11.010. Apr.

Alarabawy, R.A., Eltomey, M.A., Shehata, E.M., 2016. Volumetric study of the olfactory bulb in patients with chronic rhinonasal sinusitis using MRI. Egypt. J. Radiol. Nuclr. Med. 47 (2), 487–491. https://doi.org/10.1016/j.ejrnm.2016.02.011, 2016/06/01/.

Alshammari, M.A., Alshammari, T.K., Laezza, F., 2016. Improved methods for fluorescence microscopy detection of macromolecules at the axon initial segment. Front. Cell. Neurosci. 10, 5. https://doi.org/10.3389/fncel.2016.00005.

Anders, S., Pyl, P.T., Huber, W., 2015. HTSeq–a Python framework to work with high-throughput sequencing data. Bioinformatics 31 (2), 166–169. https://doi.org/10.1093/bioinformatics/btu638. Jan 15.

Becerra-Calixto, A., Cardona-Gómez, G.P., 2017. The role of astrocytes in neuroprotection after brain stroke: potential in cell therapy. Front. Mol. Neurosci. 10, 88. https://doi.org/10.3389/fnmol.2017.00088.

Benninger, M.S., Ferguson, B.J., Hadley, J.A., et al., 2003. Adult chronic rhinosinusitis: definitions, diagnosis, epidemiology, and pathophysiology. Otolaryngol. –Head Neck Surg. : Off. J. Am. Acad. Otolaryngol. Head Neck Surg. 129 (3 Suppl. l), S1–S32. Sep.

Biju, K.C., Mast, T.G., Fadool, D.A., Dec 5 2008. Olfactory sensory deprivation increases the number of proBDNF-immunoreactive mitral cells in the olfactory bulb of mice. Neurosci. Lett. 447 (1), 42–47. https://doi.org/10.1016/j.neulet.2008.09.050.

Burton, S.D., Urban, N.N., May 15 2014. Greater excitability and firing irregularity of tufted cells underlies distinct afferent-evoked activity of olfactory bulb mitral and tufted cells. J. Physiol. 592 (10), 2097–2118. https://doi.org/10.1113/jphysiol.2013.269886.

Cang, J., Isaacson, J.S., May 15 2003. In vivo whole-cell recording of odor-evoked synaptic transmission in the rat olfactory bulb. J. Neurosci. 23 (10), 4108–4116. https://doi.org/10.1523/jneurosci.23-10-04108.2003.

Chen, H., Lin, W., Zhang, Y., et al., Jul 26 2016. IL-10 promotes neurite outgrowth and synapse formation in cultured cortical neurons after the oxygen-glucose deprivation via JAK1/STAT3 pathway. Sci. Rep. 6, 30459. https://doi.org/10.1038/srep30459.

Chen, C., Jiang, Z., Fu, X., Yu, D., Huang, H., Tasker, J.G., Dec 24 2019. Astrocytes amplify neuronal dendritic volume transmission stimulated by norepinephrine. Cell Rep 29 (13), 4349–4361. https://doi.org/10.1016/j.celrep.2019.11.092 e4.

Chon, U., LaFever, B.J., Nguyen, U., Kim, Y., Imamura, F., 2020. Topographically distinct projection patterns of early- and late-generated projection neurons in the mouse olfactory bulb. eneuro. https://doi.org/10.1523/ENEURO.0369-20.2020. ENEURO.0369-20.2020.

Curt, A., Bruehlmeier, M., Leenders, K.L., Roelcke, U., Dietz, V., 2002. Differential effect of spinal cord injury and functional impairment on human brain activation. J. Neurotrauma 19 (1), 43–51. https://doi.org/10.1089/089771502753460222, 2002/01/01.

Dalton P. Olfaction and Anosmia in Rhinosinusitis.

DiSabato, D.J., Quan, N., Godbout, J.P., 2016. Neuroinflammation: the devil is in the details. J. Neurochem. 139 (Suppl. 2), 136–153. https://doi.org/10.1111/jnc.13607.

Doty, R.L., 2008. The olfactory vector hypothesis of neurodegenerative disease: is it viable? Ann. Neurol. 63 (1), 7–15. https://doi.org/10.1002/ana.21327. Jan.

Doty, R.L., Mishra, A., 2001. Olfaction and its alteration by nasal obstruction, rhinitis, and rhinosinusitis. Laryngoscope 111 (3), 409–423. https://doi.org/10.1097/00005537-200103000-00008. Mar.

Egaña, J.I., Aylwin, M.L., Maldonado, P.E., 2005. Odor response properties of neighboring mitral/tufted cells in the rat olfactory bulb. Neuroscience 134 (3), 1069–1080. https://doi.org/10.1016/j.neuroscience.2005.04.027.

Epstein, V.A., Bryce, P.J., Conley, D.B., Kern, R.C., Robinson, A.M., 2008. Intranasal Aspergillus fumigatus exposure induces eosinophilic inflammation and olfactory sensory neuron cell death in mice. Otolaryngol. –Head Neck Surg. : Off. J. Am. Acad. Otolaryngol. Head Neck Surg. 138 (3), 334–339. https://doi.org/10.1016/j.otohns.2007.11.029. Mar.

Eyo, U.B., Gu, N., De, S., Dong, H., Richardson, J.R., Wu, L.J., 2015. Modulation of microglial process convergence toward neuronal dendrites by extracellular calcium. J. Neurosci. 35 (6), 2417–2422. https://doi.org/10.1523/jneurosci.3279-14.2015. Feb 11.

Eyo, U.B., Haruwaka, K., Mo, M., et al., May 4 2021. Microglia provide structural resolution to injured dendrites after severe seizures. Cell Rep 35 (5), 109080. https://doi.org/10.1016/j.celrep.2021.109080.

Ferreira, F.S., Pereira, J.M.S., Reis, A., et al., 2017a. Early visual cortical structural changes in diabetic patients without diabetic retinopathy. Graefe's Arch. Clin. Exp. Ophthalmol. 255 (11), 2113–2118. https://doi.org/10.1007/s00417-017-3752-4, 2017/11/01.

Ferreira, S., Pereira, A.C., Quendera, B., Reis, A., Silva, E.D., Castelo-Branco, M., 2017b. Primary visual cortical remapping in patients with inherited peripheral retinal degeneration. Neuroimage: Clinical. 13, 428–438. https://doi.org/10.1016/j.nicl.2016.12.013, 2017/01/01/.

Galliano, E., Hahn, C., Browne, L.P., et al., 2021. Brief sensory deprivation triggers cell type-specific structural and functional plasticity in olfactory bulb neurons. J. Neurosci. 41 (10), 2135–2151. https://doi.org/10.1523/jneurosci.1606-20.2020. Mar 10.

Geramita, M., Urban, N.N., 2017. Differences in glomerular-layer-mediated feedforward inhibition onto mitral and tufted cells lead to distinct modes of intensity coding. J. Neurosci. 37 (6), 1428–1438. https://doi.org/10.1523/JNEUROSCI.2245-16.2016. Feb 8.

Gire, D.H., Franks, K.M., Zak, J.D., et al., 2012. Mitral cells in the olfactory bulb are mainly excited through a multistep signaling path. J. Neurosci. 32 (9), 2964–2975. https://doi.org/10.1523/JNEUROSCI.5580-11.2012. Feb 29.

Griff, E.R., Mafhouz, M., Chaput, M.A., 2008. Comparison of identified mitral and tufted cells in freely breathing rats: II. Odor-evoked responses. Chem. Senses 33 (9), 793–802. https://doi.org/10.1093/chemse/bjn040. Nov.

Gudis, D.A., Soler, Z.M., 2016. Chronic rhinosinusitis-related smell loss: medical and surgical treatment efficacy. Curr. Otorhinolaryngol. Rep. 4 (2), 142–147. https://doi.org/10.1007/s40136-016-0114-4.

Gwaltney Jr., J.M., 1996. Acute community-acquired sinusitis. Clin. Infect. Dis. 23 (6), 1209–1225. https://doi.org/10.1093/clinids/23.6.1209.

Hamilos, D.L., Oct 2011. Chronic rhinosinusitis: epidemiology and medical management. J. Allergy Clin. Immunol. 128 (4), 693–707. https://doi.org/10.1016/j.jaci.2011.08.004 quiz 708-9.

Hasegawa-Ishii, S., Shimada, A., Imamura, F., Sep 14 2017. Lipopolysaccharide-initiated persistent rhinitis causes gliosis and synaptic loss in the olfactory bulb. Sci. Rep. 7 (1), 11605. https://doi.org/10.1038/s41598-017-10229-w.

Hasegawa-Ishii, S., Shimada, A., Imamura, F., 2019. Neuroplastic changes in the olfactory bulb associated with nasal inflammation in mice. Mar J. Allergy Clin. Immunol. 143 (3), 978–989. https://doi.org/10.1016/j.jaci.2018.09.028. e3.

Hasegawa-Ishii, S., Imamura, F., Nagayama, S., Murata, M., Shimada, A., 2020. Differential effects of nasal inflammation and odor deprivation on layer-specific degeneration of the mouse olfactory bulb. eNeuro 7 (2). https://doi.org/10.1523/eneuro.0403-19.2020. Mar/Apr.

Hedstrom, K.L., Ogawa, Y., Rasband, M.N., 2008. AnkyrinG is required for maintenance of the axon initial segment and neuronal polarity. *J. Cell Biol.* 183 (4), 635–640. https://doi.org/10.1083/jcb.200806112. Nov 17.

Igarashi, K.M., Ieki, N., An, M., et al., 2012. Parallel mitral and tufted cell pathways route distinct odor information to different targets in the olfactory cortex. J. Neurosci. 32 (23), 7970–7985. https://doi.org/10.1523/JNEUROSCI.0154-12.2012. Jun 6.

Islam, Z., Harkema, J.R., Pestka, J.J., 2006. Satratoxin G from the black mold Stachybotrys chartarum evokes olfactory sensory neuron loss and inflammation in the murine nose and brain. Environ. Health Perspect. 114 (7), 1099–1107. Jul.

Islam, Z., Amuzie, C.J., Harkema, J.R., Pestka, J.J., 2007. Neurotoxicity and inflammation in the nasal airways of mice exposed to the macrocyclic trichothecene mycotoxin roridin A: kinetics and potentiation by bacterial lipopolysaccharide coexposure. Toxicol. Sci. 98 (2), 526–541. https://doi.org/10.1093/toxsci/kfm102.

Jacques, L., Morris, C.E., Longtin, A., Joos, B., 2014. Action potential initiation in damaged axon initial segment. BMC Neurosci. https://doi.org/10.1186/1471-2202-15-s1-p135.

Jang, J.S., Holicky, E., Lau, J., et al., Oct 24 2021. Application of the 3' mRNA-Seq using unique molecular identifiers in highly degraded RNA derived from formalin-fixed, paraffin-embedded tissue. BMC Genom. 22 (1), 759. https://doi.org/10.1186/s12864-021-08068-1.

Jenkins, S.M., Bennett, V., 2001. Ankyrin-G coordinates assembly of the spectrin-based membrane skeleton, voltage-gated sodium channels, and L1 CAMs at Purkinje neuron initial segments. *J. Cell Biol.* 155 (5), 739–746. https://doi.org/10.1083/jcb.200109026. Nov 26.

Kanaya, K., Kondo, K., Suzukawa, K., et al., 2014. Innate immune responses and neuroepithelial degeneration and regeneration in the mouse olfactory mucosa induced by intranasal administration of Poly(I:C). Cell Tissue Res 357 (1), 279–299. https://doi.org/10.1007/s00441-014-1848-2. Jul.

Karunakaran, K.D., He, J., Zhao, J., et al., 2018. Differences in cortical gray matter atrophy of paraplegia and tetraplegia after complete spinal cord injury. J. Neurotrauma 36 (12), 2045–2051. https://doi.org/10.1089/neu.2018.6040, 2019/06/15.

Kern, R.C., 2000. Chronic sinusitis and anosmia: pathologic changes in the olfactory mucosa. Laryngoscope 110 (7), 1071–1077. https://doi.org/10.1097/00005537-200007000-00001. Jul.

Kim, I.J., Beck, H.N., Lein, P.J., Higgins, D., 2002. Interferon gamma induces retrograde dendritic retraction and inhibits synapse formation. J. Neurosci. 22 (11), 4530–4539. https://doi.org/10.1523/jneurosci.22-11-04530.2002. Jun 1.

Kim, D., Langmead, B., Salzberg, S.L., 2015. HISAT: a fast spliced aligner with low memory requirements. Nat. Methods 12 (4), 357–360. https://doi.org/10.1038/nmeth.3317. Apr.

Knight, Z.A., Tan, K., Birsoy, K., et al., 2012. Molecular profiling of activated neurons by phosphorylated ribosome capture. Cell 151 (5), 1126–1137. https://doi.org/10.1016/j.cell.2012.10.039. Nov 21.

Körbler, T., Grsković, M., Dominis, M., Antica, M., 2003. A simple method for RNA isolation from formalin-fixed and paraffin-embedded lymphatic tissues. Exp. Mol. Pathol. 74 (3), 336–340. https://doi.org/10.1016/s0014-4800(03)00024-8. Jun.

Kotas Maya, E., Medzhitov, R., 2015. Homeostasis, inflammation, and disease susceptibility. Cell 160 (5), 816–827. https://doi.org/10.1016/j.cell.2015.02.010.

Lanza, D.C., Kennedy, D.W., 1997. Adult rhinosinusitis defined. Otolaryngol. Head Neck Surg. 117 (3 Pt 2), S1–S7. https://doi.org/10.1016/s0194-5998(97)70001-9. Sep.

Le, R., Esquenazi, S., 2002. Astrocytes mediate cerebral cortical neuronal axon and dendrite growth, in part, by release of fibroblast growth factor. Neurol. Res. 24 (1), 81–92. https://doi.org/10.1179/016164102101199459. Jan.

Le Bras, B., Fréal, A., Czarnecki, A., et al., Jul 2014. In vivo assembly of the axon initial segment in motor neurons. Brain Struct. Funct. 219 (4), 1433–1450. https://doi.org/10.1007/s00429-013-0578-7.

Lee, S.W., Kim, S.Y., Moon, S.Y., et al., 2021. Estimating COVID-19 infection and severity risks in patients with chronic rhinosinusitis: a Korean nationwide cohort study. Jun J. Allergy Clin. Immunol. Pract. 9 (6), 2262–2271. https://doi.org/10.1016/j.jaip.2021.03.044. e2.

Lenz, M., Eichler, A., Kruse, P., et al., 2020. Interleukin 10 restores lipopolysaccharide-induced alterations in synaptic plasticity probed by repetitive magnetic stimulation. Front. Immunol. 11, 614509. https://doi.org/10.3389/fimmu.2020.614509.

Lepousez, G., Csaba, Z., Bernard, V., et al., Jun 1 2010. Somatostatin interneurons delineate the inner part of the external plexiform layer in the mouse main olfactory bulb. J. Comp. Neurol. 518 (11), 1976–1994. https://doi.org/10.1002/cne.22317.

Lepousez, G., Csaba, Z., Bernard, V., et al., 2010b. Somatostatin interneurons delineate the inner part of the external plexiform layer in the mouse main olfactory bulb. J. Comp. Neurol. 518 (11), 1976–1994. https://doi.org/10.1002/cne.22317, 2010/06/01.

Liao, B., Hu, C.Y., Liu, T., Liu, Z., 2014. Respiratory viral infection in the chronic persistent phase of chronic rhinosinusitis. Laryngoscope 124 (4), 832–837. https://doi.org/10.1002/lary.24348. Apr.

Lindsay, R., Slaughter, T., Britton-Webb, J., et al., May 2006. Development of a murine model of chronic rhinosinusitis. Otolaryngol. –Head Neck Surg. : Off. J. Am. Acad. Otolaryngol. Head Neck Surg. 134 (5), 724–730. https://doi.org/10.1016/j.otohns.2005.11.048 discussion 731-2.

Liu, G., Froudarakis, E., Patel, J.M., et al., 2019. Target specific functions of EPL interneurons in olfactory circuits. Nat. Commun. 10 (1), 3369. https://doi.org/10.1038/s41467-019-11354-y, 2019/07/29.

Love, M.I., Huber, W., Anders, S., 2014. Moderated estimation of fold change and dispersion for RNA-seq data with DESeq2. Genome Biol 15 (12), 550. https://doi.org/10.1186/s13059-014-0550-8.

Lu, N.Z., Wardell, S.E., Burnstein, K.L., et al., 2006. International Union of Pharmacology. LXV. The pharmacology and classification of the nuclear receptor superfamily: glucocorticoid, mineralocorticoid, progesterone, and androgen receptors. Pharmacol. Rev. 58 (4), 782–797. https://doi.org/10.1124/pr.58.4.9. Dec.

Matsutani, S., Yamamoto, N., 2008. Centrifugal innervation of the mammalian olfactory bulb. Anat. Sci. Int. 83 (4), 218–227. https://doi.org/10.1111/j.1447-073X.2007.00223.x. Dec.

Meltzer, E.O., Hamilos, D.L., May 2011. Rhinosinusitis diagnosis and management for the clinician: a synopsis of recent consensus guidelines. Mayo Clin. Proc. 86 (5), 427–443. https://doi.org/10.4065/mcp.2010.0392.

Meltzer, E.O., Hamilos, D.L., Hadley, J.A., et al., Dec 2004. Rhinosinusitis: establishing definitions for clinical research and patient care. Otolaryngol. Head Neck Surg. 131 (6 Suppl. l), S1–S62. https://doi.org/10.1016/j.otohns.2004.09.067.

Miller, L.E., Bhattacharyya, N., 2022. Risk of COVID-19 infection among chronic rhinosinusitis patients receiving oral corticosteroids. Otolaryngol. Head Neck Surg. 166 (1), 183–185. https://doi.org/10.1177/01945998211006931. Jan.

Miyamichi, K., Shlomai-Fuchs, Y., Shu, M., Weissbourd Brandon, C., Luo, L., Mizrahi, A., 2013. Dissecting local circuits: parvalbumin interneurons underlie broad feedback control of olfactory bulb output. Neuron 80 (5), 1232–1245. https://doi.org/10.1016/j.neuron.2013.08.027, 2013/12/04/.

Mizuno, T., Sawada, M., Marunouchi, T., Suzumura, A., Dec 30 1994. Production of interleukin-10 by mouse glial cells in culture. Biochem. Biophys. Res. Commun. 205 (3), 1907–1915. https://doi.org/10.1006/bbrc.1994.2893.

Mori, K., Sakano, H., 2011. How is the olfactory map formed and interpreted in the mammalian brain? Annu. Rev. Neurosci. 34, 467–499.

Murphy, M.C., Conner, I.P., Teng, C.Y., et al., 2016. Retinal structures and visual cortex activity are impaired prior to clinical vision loss in glaucoma. Sci. Rep. 6. https://doi.org/10.1038/srep31464, 31464-31464.

Nagai, Y., Sano, H., Yokoi, M., 2005. Transgenic expression of Cre recombinase in mitral/tufted cells of the olfactory bulb. Genesis 43 (1), 12–16. https://doi.org/10.1002/gene.20146, 2005/09/01.

Nagayama, S., Takahashi, Y.K., Yoshihara, Y., Mori, K., 2004. Mitral and tufted cells differ in the decoding manner of odor maps in the rat olfactory bulb. J. Neurophysiol. 91 (6), 2532–2540. Jun.

Nagayama, S., Homma, R., Imamura, F., 2014. Neuronal organization of olfactory bulb circuits. Front. Neural Circ. 8, 98. https://doi.org/10.3389/fncir.2014.00098.

Ogawa, Y., Rasband, M.N., Jun 2008. The functional organization and assembly of the axon initial segment. Curr. Opin. Neurobiol. 18 (3), 307–313. https://doi.org/10.1016/j.conb.2008.08.008.

Orona, E., Rainer, E.C., Scott, J.W., Jul 1 1984. Dendritic and axonal organization of mitral and tufted cells in the rat olfactory bulb. J. Comp. Neurol. 226 (3), 346–356.

Patel, R.M., Pinto, J.M., 2014. Olfaction: anatomy, physiology, and disease. Clin. Anat. 27 (1), 54–60. https://doi.org/10.1002/ca.22338. Jan.

Peters, A.T., Spector, S., Hsu, J., et al., Oct 2014. Diagnosis and management of rhinosinusitis: a practice parameter update. Ann. Allergy Asthma Immunol. 113 (4), 347–385. https://doi.org/10.1016/j.anai.2014.07.025.

Pozzo, E.D., Tremolanti, C., Costa, B., et al., 2019. Microglial pro-inflammatory and anti-inflammatory phenotypes are modulated by translocator protein activation. Int. J. Mol. Sci. (18), 20. https://doi.org/10.3390/ijms20184467. Sep. 10.

Rasley, A., Tranguch, S.L., Rati, D.M., Marriott, I., 2006. Murine glia express the immunosuppressive cytokine, interleukin-10, following exposure to Borrelia burgdorferi or Neisseria meningitidis. Glia 53 (6), 583–592. https://doi.org/10.1002/glia.20314. Apr 15.

Rhen, T., Cidlowski, J.A., Oct 20 2005. Antiinflammatory action of glucocorticoids–new mechanisms for old drugs. N. Engl. J. Med. 353 (16), 1711–1723. https://doi.org/10.1056/NEJMra050541.

Rombaux, P., Potier, H., Bertrand, B., Duprez, T., Hummel, T., 2008. Olfactory bulb volume in patients with sinonasal disease. Am. J. Rhinol. 22 (6), 598–601. https://doi.org/10.2500/ajr.2008.22.3237. Nov-Dec.

Rosenfeld, R.M., Piccirillo, J.F., Chandrasekhar, S.S., et al., Apr 2015. Clinical practice guideline (update): adult sinusitis executive summary. Otolaryngol. –Head Neck Surg. : Off. J. Am. Acad. Otolaryngol. Head Neck Surg. 152 (4), 598–609. https://doi.org/10.1177/0194599815574247.

Sánchez-Vallecillo, M.V., Fraire, M.E., Baena-Cagnani, C., Zernotti, M.E., 2012. Olfactory dysfunction in patients with chronic rhinosinusitis, 2012 Int. J. Otolaryngol.. https://doi.org/10.1155/2012/327206, 327206-327206.

Shinozaki, Y., Shibata, K., Yoshida, K., et al., May 9 2017. Transformation of astrocytes to a neuroprotective phenotype by microglia via P2Y(1) receptor downregulation. Cell Rep 19 (6), 1151–1164. https://doi.org/10.1016/j.celrep.2017.04.047.

Skaper, S.D., Facci, L., Zusso, M., Giusti, P., 2018. An inflammation-centric view of neurological disease: beyond the neuron. Front. Cell. Neurosci. 12, 72. https://doi.org/10.3389/fncel.2018.00072.

Sobotzik, J.M., Sie, J.M., Politi, C., et al., Oct 13 2009. AnkyrinG is required to maintain axo-dendritic polarity in vivo. Proc. Natl. Acad. Sci. U. S. A. 106 (41), 17564–17569. https://doi.org/10.1073/pnas.0909267106.

Wang, M., Wang, C., Zhang, L., Feb 1 2021. Inflammatory endotypes of CRSwNP and responses to COVID-19. Curr. Opin. Allergy Clin. Immunol. 21 (1), 8–15. https://doi.org/10.1097/aci.0000000000000700.

Wickham, H., 2016. ggplot2: Elegant Graphics for Data Analysis. Springer-Verlag, New York.

Wolfensberger, M., Hummel, T., 2002. Anti-inflammatory and surgical therapy of olfactory disorders related to sino-nasal disease. Chem. Senses 27 (7), 617–622. Sep.

Xydakis, M.S., Albers, M.W., Holbrook, E.H., et al., Sep 2021. Post-viral effects of COVID-19 in the olfactory system and their implications. Lancet Neurol 20 (9), 753–761. https://doi.org/10.1016/s1474-4422(21)00182-4.

Yagi, S., Tsukatani, T., Yata, T., Tsukioka, F., Miwa, T., Furukawa, M., 2007. Lipopolysaccharide-induced apoptosis of olfactory receptor neurons in rats. Acta Otolaryngol. 127 (7), 748–753. https://doi.org/10.1080/00016480601002062. Jul.

Yamada, R., Kuba, H., 2016. Structural and functional plasticity at the axon initial segment. Front. Cell. Neurosci. 10, 250. https://doi.org/10.3389/fncel.2016.00250.

Yee, K.K., Pribitkin, E.A., Cowart, B.J., Rosen, D., Feng, P., Rawson, N.E., 2009. Analysis of the olfactory mucosa in chronic rhinosinusitis. Ann. N. Y. Acad. Sci. 1170, 590–595. https://doi.org/10.1111/j.1749-6632.2009.04364.x. Jul.